SAND2013-3737P
SAND2013-XXXX P

SANDIA NATIONAL LABORATORIES
SOLAR THERMOCHEMICAL HYDROGEN PRODUCTION (STCH) PROGRAM

QUARTERLY PROGRESS REPORT FOR JANUARY 1, 2013–MARCH 31, 2013

SUBMITTED BY: DANIEL DEDRICK, (925) 294-1552, DEDEDRI@SANDIA.GOV
TONY MARTINO, (505) 844-0652, MARTINO@SANDIA.GOV

RECIPIENT: SANDIA NATIONAL LABORATORIES

PRINCIPAL INVESTIGATOR: TONY MCDANIEL (925) 294-1440, AMCDANI@SANDIA.GOV

PROJECT TEAM: IVAN ERMANOSKI, (505) 284-0740, IERMANO@SANDIA.GOV
NATHAN SIEGEL, (570) 577-3827, NATE.SIEGEL@BUCKNELL.EDU
JIANHUA TONG,(303) 273-3053, JIANTONG@MINES.EDU
ALAN WEIMER, (303) 492-3759, ALAN.WEIMER@COLORADO.EDU

CONTENTS

FY 2013 MILESTONES/DELIVERABLES

The shaded milestones represent activities that will be conducted if an over-budget request of $200K to Sandia is granted.

Task/Milestone Description	**Status**	**Comp.**	**Plan**
Solar Thermochemical Hydrogen Production (STCH)			
Subtask 1.1: Metal Oxide Cycle Studies at Sandia National Laboratories			
Materials Discovery and Characterization			
Develop guiding principles for perovskite modification via site substitution based on documented trends of oxidation enthalpy, reduction entropy, and various other material properties reported in the literature for a small class of perovskites. A metric for success will be the discovery of one or more key indicators that show a positive correlation towards increasing the redox capacity, lowering reduction temperature, or improving kinetics.	Ongoing. Three methodologies have been devised based on thermodynamic quantities (reduction enthalpy, reduction entropy, and oxidation enthalpy), as well as perovskite structure theory. Experimental measurements are currently underway to validate and refine the design principles.	30%	2/13
Synthesize at least 50 different perovskite compounds. These materials will be identified by application of the “guiding principles” established in the previous task. Material synthesis to be conducted in collaboration with Colorado School of Mines (CSM). A metric of success will be to synthesize 500 mg each of phase-pure materials.	Synthesized between 200–1,000 mg sized samples of 45 different perovskite compounds from 9 elements (Al, Cr, Ce, Fe, La, O, Sr, Ti, Zr). Most compounds showed expected crystallographic phases: either cubic, orthorhombic, or hexagonal lattice structures. Most compounds were also found to be single phase (i.e., little to no impurity content).	95%	6/13

Task/Milestone Description	Status	Comp.	Plan
Characterize the thermodynamic and kinetic performance of synthesized perovskites using Sandia's rapid thermal-cycling stagnation flow reactor and thermo-gravimetric analysis available at both Sandia and CSM. A metric for success will be the discovery of a perovskite formulation that can split water, thermally reduce at a temperature less than 1,350 ºC, and has twice the capacity of undoped ceria (> 100 µmoles H_2/g).	Reported in Q1FY13 the discovery of Sr- and Mn-doped $LaAlO_3$ (SLMA) that outperforms CeO_2. SLMA reduces at T < 1350 ºC and produces > 300 µmoles H_2/g (better than 9 times more than CeO_2 when reduced at 1,350 ºC). In Q2FY13, we characterized kinetics for Fe-doped calcium titanate ($CaTi_{1-x}Fe_xO_3$) and found water-splitting (WS) activity similar to CeO_2. This is the first demonstration of a perovskite formulated from earth-abundant ores that can split water (i.e., produce H_2), though no real performance gains relative to CeO_2 were evident.	80%	9/13
Reactor Development			
Material conveying performance will be measured using the existing engineering test stand, under ambient conditions of temperature and pressure. Metrics of success are the ability to convey material at 8 g/s in the 3-inch auger and 30 g/s in the 8-inch auger.	Particle transport assessed using a 3-inch auger designed for heat recuperation (narrow finned, double helix). The 3-inch auger transports 8 g/s at 4 RPM, and 40 g/s at 20 RPM. Achieved particle conveyance rates that exceed reactor design requirement. Postponed the 8-inch test.	100%	9/13
Upgrade the engineering test stand for vacuum-compatible operation up to 200 °C. A preliminary design for a vacuum-capable prototype operating up to 900 °C will be completed.	In progress. Conceived a design that allows for high-vacuum separation between the stationary and rotating chamber walls of the reactor vessel, while permitting *external* drive via conventional gears and bearings. These concepts are critical to developing the engineering test stand and will be validated this FY.	25%	9/13
Characterize engineering test stand under conditions of vacuum (10 Pa < p < 10 kPa), gas flow, and increased temperature (T < 200 °C). Metrics of success are the ability to convey material at 30 g/s in the entire design range. The results of these tests will be used to finalize the 900 °C prototype design.	Planning stage.	0%	9/13

Task/Milestone Description	**Status**	**Comp.**	**Plan**
System Analysis			
Develop system-level designs and analyses of central-receiver-based platforms that include additional detail related to the balance of system components for a particle reactor-based hydrogen production system having an annual average solar-to-hydrogen efficiency in excess of 20% (as opposed to 14% in FY12).	Estimated the cooling requirements for the beam-down optic reflector using a heat transfer model. Cooling the secondary can be accomplished via forced air or water cooling methods.	60%	7/13
Assess the cost of hydrogen production from a particle reactor using the H2A3 tool on either a parabolic dish or central receiver platform, to include sensitivity studies showing how system costs can be impacted by technology improvement of major subsystem costs, e.g., heliostats.	Completed multiple iterations of the H2A3 analysis for a dish-based production facility. Continuing to refine the analysis in collaboration with SA, Inc. Current estimate for high-volume production cost in 2020 is \$8.56/kg H_2. We have identified that reactor efficiency (STHE) is the most significant cost driver.	80%	9/13
Standardized Screening Method			
Retrofit the stagnation flow reactor to operate at pressure > 1,500 Torr and water concentration ≤ 85 volume %.	5 months after authorization.		
Design and implement a material characterization protocol that adheres to the principles of "best practice." A flow chart describing key characterization methods to facilitate materials development will be derived and vetted. At a minimum, the flow chart will include benchmarks and recommendations for assessing kinetics, redox capacity, limiting reduction temperature, and cycle durability.	8 months after authorization.		

Task/Milestone Description	Status	Comp.	Plan
Subtask 1.2: ALD Active Thin Films/Support Materials for Ferrite/Hercynite Thermochemical Redox Cycle/Solar Reactor			
Hercynite Redox Nanostructured Materials and Isothermal Cycling			
Synthesize a cobalt ferrite/alumina hercynite active material by atomic layer deposition (ALD) using polymer templates. Demonstrate isothermal redox water-splitting in a stagnation flow reactor at a temperature of 1,350 ºC yielding a H_2 production per gram of total mass of active material greater than 100 µmoles/g.	Demonstrated March, 2013. Isothermal redox carried out at 1,350 °C produced 217.3 µmole H_2/g active material for 50% steam concentration at a total pressure of 760 Torr.	100%	9/13
Theoretical studies using density functional theory (DFT) will be used to develop an understanding of the isothermal redox cycling process. Evaluate design and efficiency trade-offs between isothermal and conventional temperature-variant thermochemical redox cycle operation using hercynite.	DFT has shown that Fe has the lowest activation barrier for cation migration through the lattice of the spinel, followed by Co, then followed by Ni. Isothermal redox thermodynamics has been developed based on chemical potential and is being reviewed.	70%	6/13
Multi-Tube Solar Receiver			
On-sun demonstration at NREL HFSF of cobalt ferrite/alumina hercynite cycle active materials using polymer templates. Demonstrate isothermal redox water-splitting yielding a H_2 production per gram of total mass of active material greater than 100 µmoles/g.	Synthesizing materials for the on-sun test.	10%	9/13
A model of the tubular reactor will be developed in FLUENT and used to simulate reactor performance. We will evaluate the impact on efficiency of isothermal redox cycling vs. conventional thermochemical redox. A 4.5-kW multi-tube solar reactor will be designed along with a designed solar flux for a predicted dynamic efficiency of greater than 5%.	A dynamic model has been developed and simulations are continuing for evaluating isothermal redox vs. conventional temperature-swing redox for the "hercynite cycle" materials contained in an absorbing cavity solar reactor. Preliminary efficiencies greater than 5% have been calculated for a 4.5-kW receiver.	70%	9/13

SUBTASK 1.1: METAL OXIDE CYCLE STUDIES AT SANDIA NATIONAL LABORATORIES

BACKGROUND

The conversion of solar radiation into a chemical fuel such as hydrogen is an engineering challenge; however, unlike solar-derived electricity or heat, it is easier and more efficient to transport and store hydrogen. This point is important because energy demand is rarely matched to incident solar radiation, either spatially or temporally. Two-step solar-driven thermochemical processes based on non-volatile metal oxide cycles are an attractive technology for producing hydrogen from water because of the potential to operate at high solar-to-chemical conversion efficiency with moderate operational demands on land and water resources. Conceptually, solar energy is collected and concentrated using heliostats. This can be accomplished on small scales with trough- and dish-type receivers operating at tens of kilowatts, to large-scale central receivers operating at tens of megawatts. Incident solar radiation can thus be converted to high-temperature process heat and then used to drive a thermochemical water-splitting reaction.

OBJECTIVE

The overall objective of this subtask is to develop a practical solar-driven hydrogen production system based on a non-volatile metal oxide cycle using a particulate media. This process involves the development of a high-temperature particle conveying and reactor system, making improvements to the reactant materials, expanding our understanding of the underlying material thermodynamics and kinetics, updating system performance calculations, and developing economics models.

MATERIALS DISCOVERY AND CHARACTERIZATION

Point of Contact: Tony McDaniel

PROJECT STATUS

Perovskite oxides (ABO_3) are a largely unexplored class of materials in solar fuel applications. In Q2FY13 we continued to synthesize and characterize a small number of compounds that were identified largely through experience and chemical intuition. In a separate activity, we also evaluated the impact of operating a thermochemical cycle isothermally, as opposed to having the reduction temperature well above the oxidation temperature. We assessed the impact on cycle efficiency using CeO_2 as a representative material. We will discuss the status of these two activities separately.

Novel Perovskites for STCH

A wet-chemistry method of EDTA acid and citric acid combined complexing was used to synthesize mixed oxide powders of $SrCe_{1-x}Fe_xO_{3-\delta}$ (x = 0.0, 0.1, 0.2, and 0.3). In addition, a solid-state reaction method was used to synthesize $CaTi_{1-x}Fe_xO_{3-\delta}$ (x = 0.0, 0.1, 0.2, and 0.3). The goal here is to explore perovskite materials that can be formed from more earth-abundant elements, as well as develop methods for efficiently synthesizing prospective formulations.

The wet method is an involved process that takes several days and constant monitoring to complete. Essentially, proper amounts of nitrate salts for each componential metal cation are mixed into a beaker in order to produce the desired amount of oxide powder. EDTA acid and citric acid are then added to the beaker in the appropriate molar proportions, followed by careful addition of ammonium hydroxide and distilled water. The mixture is then continuously stirred and slowly heated to 85 °C until enough water has evaporated to produce a sticky gel. The gel is then removed from the beaker and dried in an oven for 48 h, producing a solid material that is ground into a fine powder. To complete the synthesis, powders are calcined at 950 °C for 10 h and 1350 °C for an additional 5 h. While the wet method produces high-quality samples, it is desirable to find an approach that can produce materials more efficiently and cost effectively.

The solid-state reaction method still takes several days to complete per an individual compound, but requires less supervision, and is more easily automated and scaled down. Here, proper amounts of solid precursors such as carbonate and binary oxide powders are added to a plastic bottle with isopropanol as a solvent for grinding (e.g., when making $CaTi_{1-x}Fe_xO_{3-\delta}$, $CaCO_3$, TiO_2, and Fe_2O_3 are used as precursors). Small yttria-stabilized zirconia (YSZ) beads are then added to the bottle and the mixture is milled at low energy for 48 h. After removing the grinding beads and drying the slurry, the resultant powder is calcined at 1350 °C for 20 h, with an intermediate interval of manual grinding in between. The solid-state reaction approach is more amenable to high-throughput synthesis because grinding can be accomplished in parallel using milling machines with multiple pods. In addition, this approach is easily scaled down to produce small amounts of materials (200-mg quantities).

Both methods produce crystalline material. Illustrated in Figure 1 are *x*-ray diffraction (XRD) patterns for $SrCe_{1-x}Fe_xO_{3-\delta}$ synthesized by the wet method and $CaTi_{1-x}Fe_xO_{3-\delta}$ by the solid-state reaction method. The patterns clearly indicate the perovskite phase was formed for each of the compositions. We are still analyzing the XRD data to identify crystal structure and the extent of phase purity.

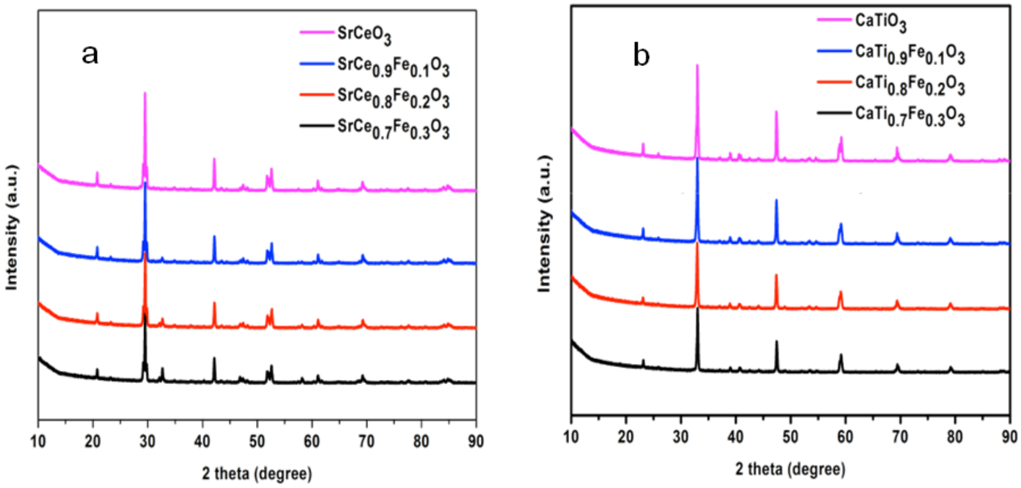

Figure 1. XRD patterns for powders of SrCe1-xFexO3-δ (a) and CaTi1-xFexO3-δ (b) (x = 0.0, 0.1, 0.2, and 0.3). The final annealing temperature was 1,350 ºC.

A critical first assessment for material viability in solar fuel applications is to determine the extent of oxygen deficiency that can be achieved under conditions of rapid heating and constant oxygen activity. The oxygen deficiency for ceria and perovskites is represented by (δ) in the chemical formula (i.e., the subscript 2-δ for ceria and 3-δ for perovskite). The larger the value of (δ) in the reduced state, the more H_2 you can expect to make per a redox cycle. Presented in Figure 2 is the oxygen uptake and release measured for $CaTi_{0.7}Fe_{0.3}O_{3-\delta}$ exposed to a constant 0.2 mbar O_2 partial pressure in helium flow and heated at 7 °C/s to a thermal reduction temperature (T_R) of 1,350 °C. Rapid heating in Sandia's stagnation flow reactor is accomplished by irradiation from a near-infrared laser. In this figure, a positive production rate indicates O_2 released by the solid, and a negative rate indicates O_2 incorporation.

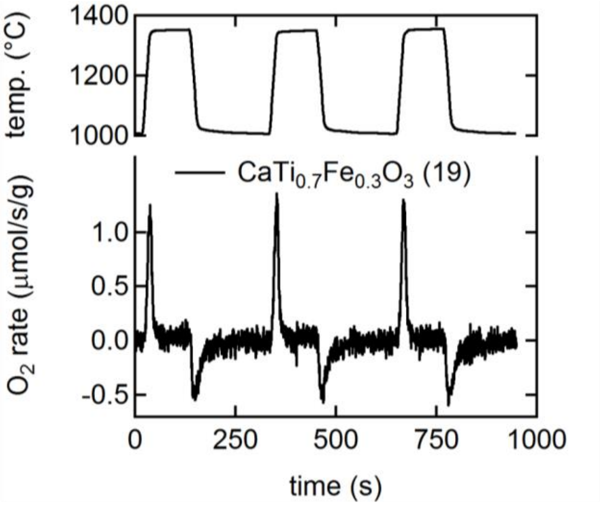

Figure 2. Rate of O_2 uptake (+ values) or release (- values) as a function of time and temperature at 0.2 mbar O_2 pressure. The total amount of O_2 absorbed or released per cycle in μmol/g is shown in the parenthesis and is directly related to δ.

The data in Figure 2 show that a perovskite formulated entirely from earth-abundant ores (i.e., containing Ca, Ti, and Fe) is found to be redox active (a novel observation because not all perovskites are redox active). The total amount of oxygen that leaves the solid under these conditions of thermal reduction (T_R = 1,350 °C and constant O_2 activity) is similar to CeO_2 (see Table 1). Therefore, we would expect the redox cycle performance and total amount of H_2 produced to also be similar.

Table 1. Total amount of O_2 and H_2 produced during thermal reduction and oxidation in 40 vol% H_2O. [a]$CaTi_{0.7}Fe_{0.3}O_3$ reduced at 1400 °C prior to water splitting (see Figure 3).

Material	T_R (°C)	O_2 (μmole/g)	T_{WS} (°C)	H_2 (μmole/g)
CeO_2	1,350	20	1,000	32
$CaTi_{0.7}Fe_{0.3}O_3$	1,350	19	[a]1,100	39

The evolution of H_2 when exposing the reduced $CaTi_{0.7}Fe_{0.3}O_{3-\delta}$ to H_2O at conditions typically used in concentrating solar power (CSP) thermochemical cycles demonstrates that water-splitting (WS) chemistry is favorable. Shown in Figure 3 is the H_2 production rate for this perovskite measured over previously reduced oxide. We note that the $CaTi_{0.7}Fe_{0.3}O_{3-\delta}$ was re-oxidized under a constant flow of water that swept the H_2 gas from the reactor. This creates a condition that maximizes the thermodynamic driving force for re-oxidation in the SFR. There are few materials other than ceria and ferrite (including hercynite) that have demonstrated WS capability, and within a few short months we have identified two families of perovskites ($Sr_xLa_{1-x}Mn_yAl_{1-y}O_3$ and $CaTi_{1-x}Fe_xO_3$). We feel strongly that many more perovskite formulations will exhibit this behavior and their performance will surpass both ceria and ferrite chemistries. Unfortunately, this particular Fe-doped calcium titanate performs similarly to ceria (see Table 1). This means that unless we can significantly increase the redox capacity by adding more Fe, further development of this formulation is not warranted.

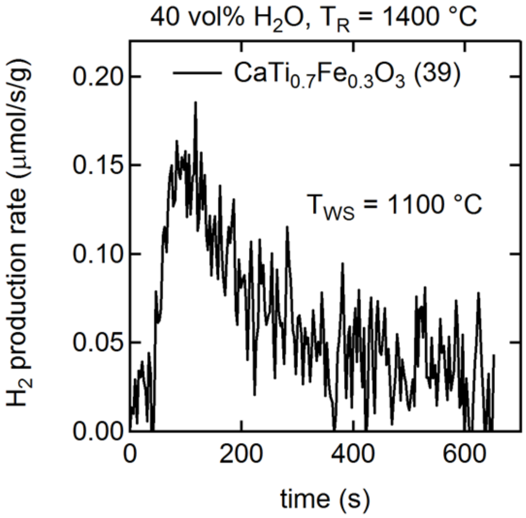

Figure 3. Production rate of H_2 as a function of time over previously reduced $CaTi_{0.7}Fe_{0.3}O_{3-\delta}$ perovskite. T_{WS} is the oxidation temperature; the total amount of H_2 produced in μmol/g is shown in parentheses.

Evaluation of Isothermal WS on CeO_2

The question of running a solar thermochemical WS cycle isothermally has been posed, and here we describe the results of kinetic measurements to assess the impact of this choice on cycle efficiency. In the following section on Reactor Development, we will discuss the impact of isothermal operation on solar-to-hydrogen efficiency (STHE) for the entire system, as determined by detailed thermodynamic modeling. This work was motivated by recent H2A3 analysis of the Sandia particle reactor that revealed the importance of STHE in determining H_2 production cost. Relative to a baseline cost projection of \$35/kg H_2 in 2015 for a 100,000 kg H_2/day dish-based plant, the STHE metric is fully 75% of this delivery price (ca. \$26/kg H_2 assuming an increase in STHE from 6% to 31% needed to reach the ultimate cost target). Clearly the STHE is by far the biggest cost driver, even more than the price reduction gained by decreasing the capital cost of the solar concentrator from \$140/m^2 to \$70/m^2. Thus, any concept that limits or negatively impacts the STHE must be heavily scrutinized.

CeO_2 was used to assess the impact on WS cycle performance. Under normal circumstances, ceria is reduced at $T_R \geq 1{,}500$ °C, and then re-oxidized by WS between 900–1,000 °C ($\Delta T > 500$ °C). This produces roughly 140 μmol H_2/g CeO_2. It is impractical to operate the WS chemistry isothermally at 1,000 °C, simply because the extent of oxygen non-stoichiometry (δ) for CeO_2 is too small at this temperature. Therefore, the idea is to conduct WS at higher temperature, close to the T_R (> 1,500 °C). It is still possible to oxidize previously reduced CeO_2 at T ~ 1,400 – 1,500 °C provided enough H_2O is present to ensure thermodynamic favorability. However, the amount of H_2 made is severely limited because the driving force for oxidation is smaller at higher temperature. In practice, isothermal operation is analogous to pressure-swing operation. To reduce CeO_2, the O_2 partial pressure is decreased to some small amount by sweeping with an inert gas (He or Ar); then steam is injected to increase the partial pressure (activity) of O_2 such that the material re-oxidizes. Even though the cycle may operate at constant total pressure, the O_2 partial pressure swings back and forth, producing H_2 along the way.

Presented in Figure 4 are the results of our kinetic measurements on CeO_2. The top panel shows the H_2 production rate for a single isothermal cycle operating at 1,450 °C ($\Delta T = 0$ °C), and the bottom panel for WS at 950 °C after reduction at 1,500 °C ($\Delta T = 550$ °C). First considering the data in the bottom panel (i.e., normal temperature-swing operation), the total amount of H_2 produced in a single cycle is 140 μmol H_2/g CeO_2 (the area under the curve between 0 and 500 s shown in parenthesis). In addition, the amount of O_2 co-produced at this WS condition (Figure 4, dashed line) is at or below the detection limit. Considering the isothermal data (top panel), when the WS temperature is raised to 1,450 °C the shape of the H_2 production curve changes and the O_2 production rate rises above the detection limit. We have determined that a catalytic process occurring on hot surfaces other than CeO_2 in the stagnation flow reactor splits H_2O continuously and, as a result of our unique reactor configuration and method of operation, the co-evolved H_2 and O_2 gases can be detected. Although tempting, it is not practical to generate H_2 in this way. But it does raise the possibility that *any* isothermal process operating at such high temperatures will generate both H_2 and O_2 in the same process stream. The H_2 yield from the stoichiometric reaction (grey shaded area representing the oxidation of CeO_2) is 44 μmol H_2/g CeO_2. This value is 70% less than the amount of H_2 produced by temperature-swing operation and will result in a similar decrease in the STHE for a process operating as such. As will be discussed in the next section, isothermal operation yields by far the lowest STHE in the Sandia particle reactor under what we consider achievable operating conditions.

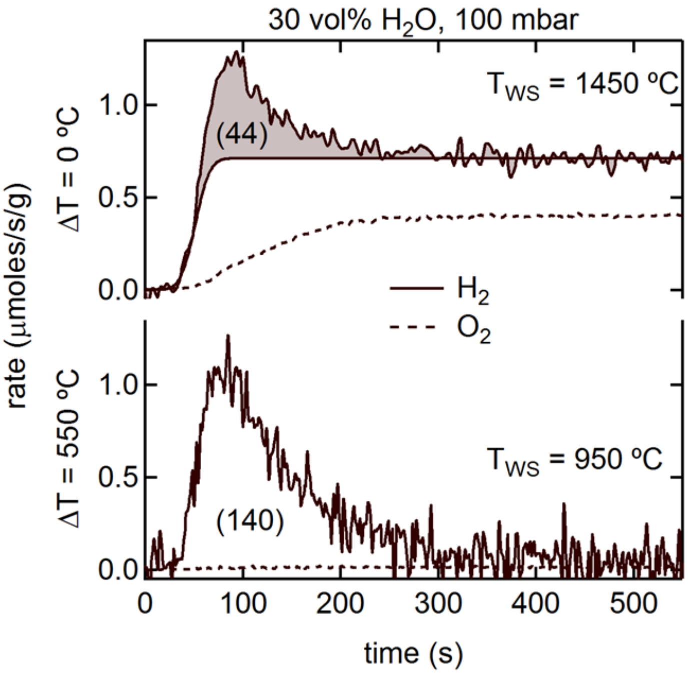

Figure 4. Production rates for H_2 and O_2 as a function of time. (Top) Isothermal WS cycle, (bottom) temperature-swing WS cycle. Both H_2 and O_2 are produced during isothermal WS by a catalytic process on surfaces other than CeO_2 (see text).

PLANS FOR NEXT QUARTER AND KEY ISSUES

In Q3FY13 we will continue to synthesize and screen perovskite formulations.

REACTOR DEVELOPMENT

Point of contact: Ivan Ermanoski

PROJECT STATUS

In Q2FY13, the reactor development work focused on three areas:

1. Extending the reactor models.
2. Developing a model to estimate recuperator performance.
3. Upgrading the engineering test stand and designing a vacuum system.

Anticipating the use of a recently discovered perovskite material ($Sr_xLa_{1-x}Mn_yAl_{1-y}O_3$) and the potential for considerable improvement in reactor performance, we have extended reactor numerical models in two important ways. The first is the ability to extract oxide thermodynamic properties from experimental data and to use these results to model reactor efficiency. The second is a detailed accounting of the energy need for feedstock steam production and heating. This accounting is important in order to model operation for any $\Delta T = T_{TR}-T_{WS}$ (difference between thermal reduction, TR, and water splitting or H_2 production, WS, temperatures) rather than the experimentally validated $\Delta T = 400$ K. This work is still in progress and awaits detailed thermodynamic information for the perovskites, but has led to several interesting and encouraging results—namely, a better defined optimal operating point for the reactor, as well as revealing new modes of operation that explore less-optimal heat recuperation scenarios.

One key result is the discovery of an optimal temperature difference (ΔT_{opt}) for operating at any given recuperator effectiveness (ε_{HR}) and thermal reduction pressure (p_{TR}). The thermal reduction pressure is the partial pressure of O_2 in the reduction zone at T_{TR}. Figures 5–7 show the solar-to-hydrogen efficiency (STHE, η) as a function of reduction pressure for several values of ε_{HR}. The ΔT is different in each of these figures: 190 K in Figure 5, 220 K in Figure 6, and 400 K in Figure 7. In Figure 5, we see that for a modest recuperator effectiveness value of $\varepsilon_{HR} = 50\%$ (red curve) and moderate reduction pressure $p_{TR} = 100$ Pa at $\Delta T = 190$ K, the STHE $\eta = 19.2\%$. This happens to be the ΔT_{opt} for this reduction pressure and recuperator effectiveness using CeO_2 as the active oxide. For example, at $\Delta T = 220$ K with the same reduction pressure and recuperator effectiveness (red curve in Figure 6) the $\eta = 18.7\%$, and at 400 K (red curve in Figure 7) the $\eta = 15.1\%$. Therefore, our calculations reveal that $\eta_{190\,K} > \eta_{220\,K} > \eta_{400\,K}$. Similarly, for a higher recuperator effectiveness of $\varepsilon_{HR} = 70\%$ (light blue curves in Figures 5–7) and $p_{TR} = 100$ Pa, ΔT_{opt} has now increased to 220 K ($\eta_{220\,K} > \eta_{400\,K} > \eta_{190\,K}$). By expanding the model to include a more detailed accounting of the energy required for heating the active material between T_{TR} and T_{WS}, as well as the energy required to produce enough steam to ensure thermodynamic favorability for oxidation, we can now quantify the tradeoff between these two major sensible heat loads. Essentially, these results show that, to operate at peak STHE, the ΔT must be chosen to minimize the energy required to heat both material and steam, which is ultimately determined by the thermodynamic driving force for oxidation and the extent of reduction or oxygen deficiency (δ) achievable in the solid.

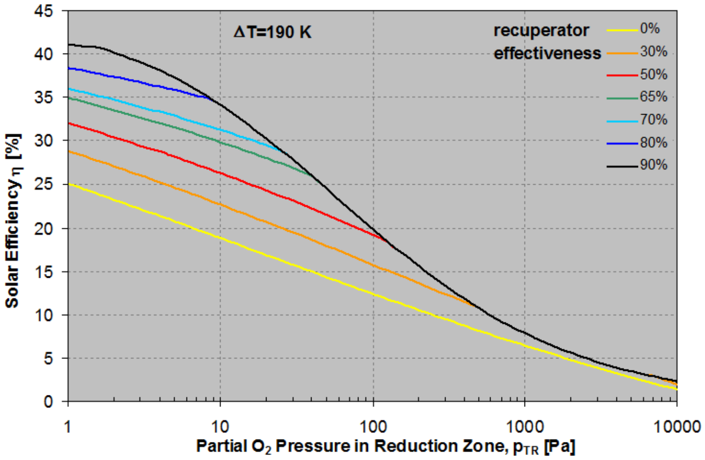

Figure 5. Solar efficiency (STHE) as function of reduction pressure at ΔT = 190 K.

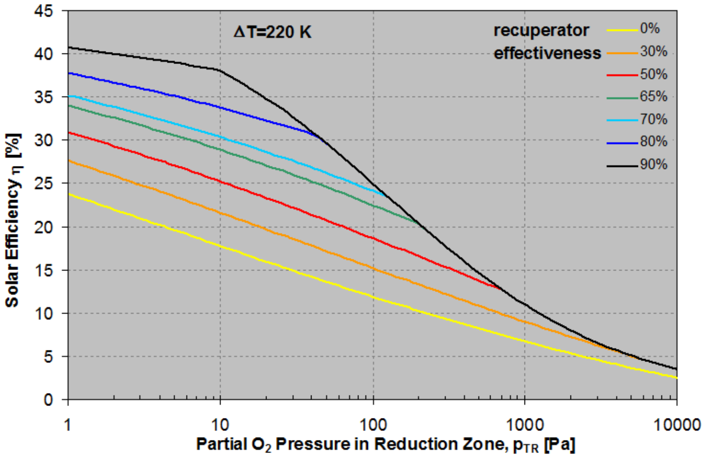

Figure 6. Solar efficiency (STHE) as function of reduction pressure at ΔT = 220 K.

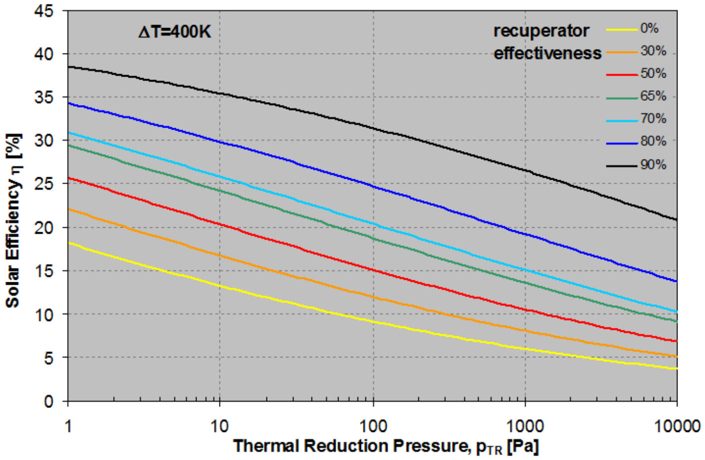

Figure 7. Solar efficiency (STHE) as function of reduction pressure at ΔT = 400 K.

One final note regarding isothermal operation, which is illustrated in Figure 8 where ΔT = 0 K. While possible, isothermal operation yields by far the lowest efficiency (STHE) except for low recuperation and a reduction pressure of pTR = 1 Pa; a value that is unattainable in practice for a large system either through pumping or inert purge of the reduction chamber. In Figure 8, all recuperator effectiveness curves (colored lines) are stacked on each other, and, since ΔT=0, operation is the same irrespective of recuperation; therefore, disregard the graph legend. The reason for such low efficiency is the excessive amount of steam and related heat loads required for isothermal operation. As was shown in the previous section, oxidizing CeO_2 at ca. 1,500 °C reduces the STHE simply because the thermodynamic driving force to put oxygen atoms back into the solid (thus creating H_2) is drastically diminished. In fact, to drive WS at these conditions ultimately requires a very large amount of excess steam, which according to Figure 8 causes the STHE to plummet. In addition, the solar energy input required for steam production and other heating loads under isothermal conditions is independent of reactor mechanical details, and depends only on material thermodynamics (i.e., the thermal reduction temperature and pressure).

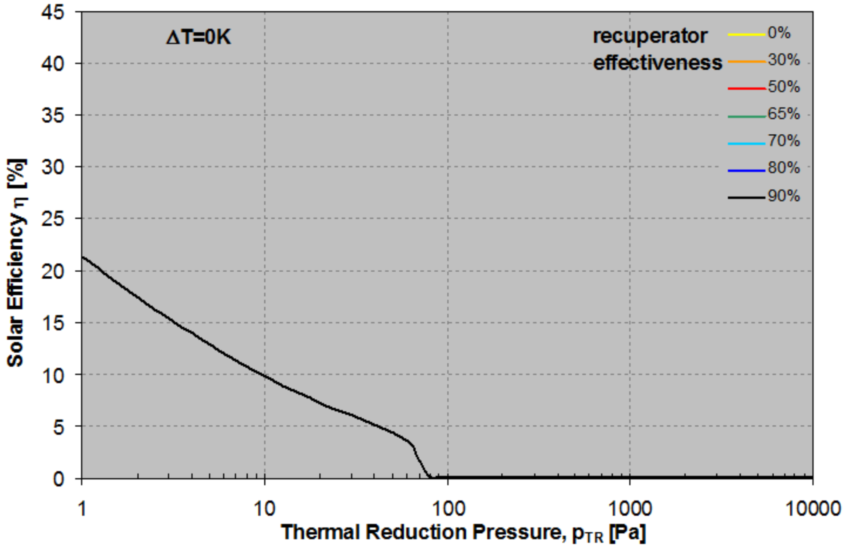

Figure 8. Solar efficiency (STHE) as function of reduction pressure at ΔT = 0 K.

We note that these calculations were performed using ceria thermodynamic parameters, but this extended model is capable of calculating reactor efficiencies for other materials as well. Furthermore, the thermodynamic model used for these new calculations is not the same as used previously (based on data from Panlener et al. (*J. Phys. Chem. Solids*, **36** 1975, 1213), but relies on a more recent analysis by Zinkevich et al. (*Solid State Ionics*, **177** 2006, 989). This model yields lower overall efficiencies than the Panlener model, but we believe it to be more accurate. It does not affect relative efficiency comparisons for various operating conditions.

Regarding the reactor design activity, having successfully validated the first auger design for particle conveying (we exceeded the 4 g/s requirement by a factor of approximately five), we modeled recuperator performance using the salient geometric parameters of the working auger and a basic heat transfer approach. The main outcome of this activity was a first estimate of the recuperator size necessary to achieve ε_{HR} = 50% in a 5-kW device: roughly 70 cm in length and 20 cm in diameter. This size is appropriate for incorporation into our engineering test stand. Furthermore, the model shows that recuperator performance strongly depends on auger geometry. This means that modest modifications in auger geometry (most importantly flight spacing and depth) would lead to a considerable decrease in recuperator size, or increase in efficiency, whichever is deemed more important. Considering the exceptional performance of the first auger design, it is reasonably safe to assume that an auger better optimized for heat transfer would still perform satisfactorily as a particle conveyor.

While these heat transfer results are basic and preliminary, they also rest on the conservative assumption that the only mechanism of heat transfer is particle bed thermal conductivity. Any internal convective motion of the bed imparted by the rotating casing (and potential increase of heat transfer) was neglected in the calculation but would certainly improve the recuperator effectiveness.

Finally, to facilitate future measurements, we upgraded the engineering test stand with the capability to reverse casing rotation. This upgrade will enable more expeditious replacement of augers, scoops, and other interchangeable components. We have also continued the design of a vacuum system necessary to perform conveying tests under conditions of decreased gas pressure and, in the future, increased temperature and pressure differences.

PLANS FOR NEXT QUARTER AND KEY ISSUES

In Q3FY13 we plan to focus on reactor modeling and design of the vacuum-compatible engineering test stand.

SYSTEMS ANALYSIS

Point of contact: Nathan Siegel

PROJECT STATUS

In Q2FY13 we provided additional input to the H2A3 analysis of the dish-based particle reactor, and initiated the thermal design of a high-concentration beam-down mirror that is required to deploy the particle reactor on a central receiver platform. The H2A3 analysis effort was led by Strategic Analysis, Inc., and they have made revisions to models previously developed by Sandia. Although work continues on the dish-based H2A3 analysis, it is likely nearing completion. An H2A3 analysis for a tower-based configuration was originally planned for Q2FY13, but this task was delayed to allow time to assess the outcome of the dish-based analysis and to evaluate the technical feasibility of some of the critical components (e.g., beam-down mirror) in the central receiver-based particle reactor system.

The beam-down central receiver being developed for the particle reactor is unique in that the terminal concentrator (beam-down optic mounted on the tower) is exposed to relatively high incident concentrated solar flux (~200 kW/m^2). It is anticipated that mirror designs based on back-silvered, low-iron glass can tolerate this level of heat flux, but only if they are cooled such that the maximum temperature in the mirror remains below 100 °C. Since the terminal concentrator is a crucial component in the central receiver configuration of the particle reactor concept, we developed a thermal model to evaluate the temperature distribution in the terminal concentrator as a function of the degree of achievable cooling on the bottom, glass side, and top, finned side. A schematic of a back silvered glass mirror is shown in Figure 9.

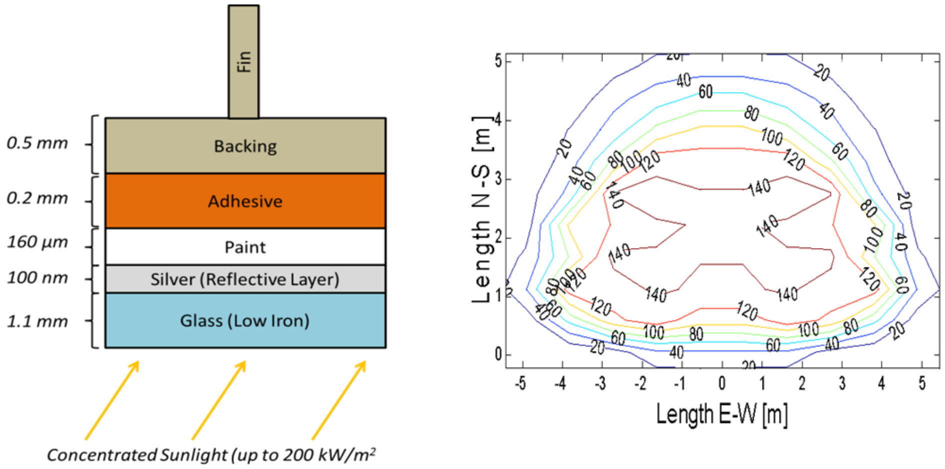

Figure 9. (left) The structure of a back-silvered glass mirror and (right) the flux distribution on the mirror in our base-case central receiver configuration (flux values are in kW/m^2).

Most of the heating takes place at the interface between the glass and silver reflector and is a function of the reflectivity of the silver itself. Additional heating also occurs volumetrically within the glass. The temperature of the mirror during operation is primarily controlled by the rate at which heat can be removed from the front and back surfaces. Our analysis shows that minimizing heat transfer resistance through the back of the mirror is essential to maintaining a low operating temperature when exposed to high flux. Ideally, natural convection would be sufficient to remove all heat from the mirror, avoiding the need for forced-air cooling. Unfortunately, our models show that the expected rate of heat removal via natural convection is too low.

The combination of bonding fins to the back of the mirror assembly and forcing air across them with a fan is sufficient to remove excess heat from the mirror and maintain an operating temperature below 100 °C when incident flux is 200 kW/m^2. Figure 10 shows that a flow of 5 m^3/s produces a sufficiently large convection coefficient (greater than the minimum required to maintain 100 °C operation) at any cooling air flow rate above 5 m^3/s if the fin pitch is 1 cm. For larger values of fin pitch cooling is sufficient when operating above the line labeled “Minimum Conv. Coeff.”

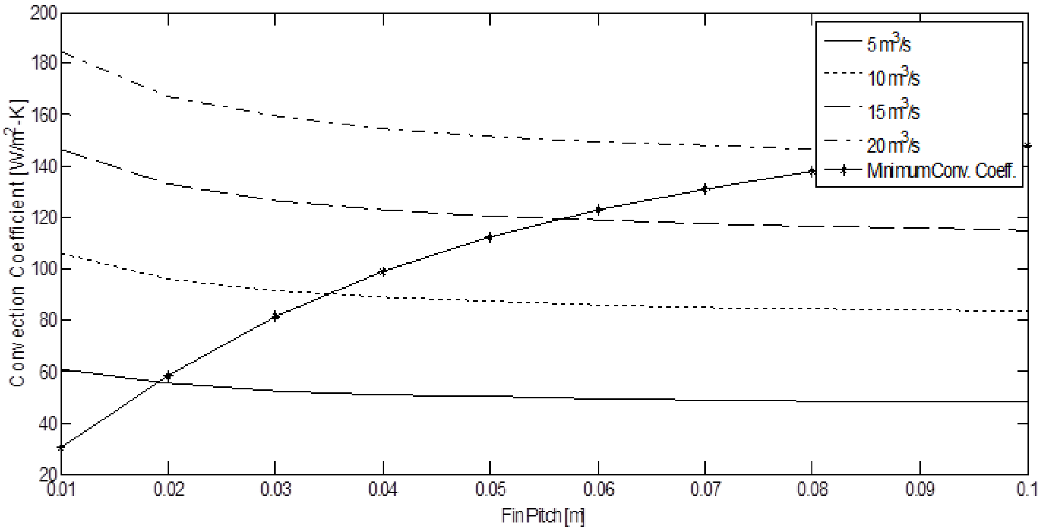

Figure 10. Estimated convection coefficient in the likely cooling flow rate range.

PLANS FOR NEXT QUARTER AND KEY ISSUES

In the next quarter we plan to implement a finite element based thermal model of the beam-down reflector and to design a prototype for experimental evaluation on Bucknell's solar simulator. In addition, we also plan to begin working on the H2A3 analysis for the central receiver configuration of the particle reactor. We hope to collaborate with Strategic Analysis, Inc. on the H2A3 analysis.

STANDARDIZED SCREENING METHOD

Point of contact: Tony McDaniel

PROJECT STATUS

No activity; awaiting authorization and additional funding.

PLANS FOR NEXT QUARTER AND KEY ISSUES

No activities planned unless authorization is granted.

PUBLICATIONS/PRESENTATIONS

Scheffe, J. R., McDaniel, A. H., Allendorf, M. D. & Weimer, A. W. "Kinetics and Mechanism of Solar-Thermochemical H_2 Production by Oxidation of a Cobalt Ferrite–Zirconia Composite." *Energy Environ. Sci.* **6,** 963 (2013).

Ermanoski, I., Siegel, N. P. & Stechel, E. B. “A New Reactor Concept for Efficient Solar-Thermochemical Fuel Production.” *J. Solar Energy Engineering* **135,** 031002 (2013).

Siegel, N. P., Miller, J. E., Ermanoski, I., Diver, R. B. & Stechel, E. B. “Factors Affecting the Efficiency of Solar Driven Metal Oxide Thermochemical Cycles.” *Industrial & Engineering Chemistry Research* **52,** 3276–3286 (2013).

McDaniel, A. H. et al. “High Temperature Splitting of Water and Carbon Dioxide Using Complex Oxides as a Route to Solar Fuels.” Invited talk presented at the 245th meeting of the American Chemical Society, April 2013, New Orleans, LA.

SUBTASK 1.2: ALD ACTIVE THIN FILMS/SUPPORT MATERIALS FOR FERRITE/HERCYNITE THERMOCHEMICAL REDOX CYCLE/SOLAR REACTOR

OBJECTIVE

The overall objective of this subtask is to continue with the encouraging investigation of active ferrite thin films prepared by atomic layer deposition (ALD) for the splitting of water via a solar thermochemical hercynite redox cycle. A key aspect is the in-situ preparation of an active ultra-thin and highly porous, large-pore-size reactive alumina substrate prepared by ALD using a polymer template. The ferrite reacts with alumina providing stable hercynite which has been demonstrated to form a reduced intermediate at temperatures ~ 150 ºC below that of conventional ferrites. Thin films of active materials reduce diffusion and thermal resistances. Investigation includes the formation of the substrate, deposition of active ferrite films, the isothermal cycling of the films under a controlled environment, an improved understanding of the underlying materials thermodynamics and kinetics, efficiency of the solar reactor and an on-sun demonstration of a single-tube isothermal solar redox reactor.

HERCYNITE REDOX NANOSTRUCTURED MATERIALS AND ISOTHERMAL CYCLING

Point of contact: Alan W. Weimer

PROJECT STATUS

Hercynite Materials and Isothermal Water-Splitting

This quarter, efforts focused on producing skeletal alumina substrate materials for use in the "hercynite cycle," deposition of $CoFe_2O_4$ on standard alumina catalyst supports, and testing the effects of steam pressure on isothermal water splitting (ITWS).

For the past few quarters, we have been working on coating "DOWEX" particles, composed of polystyrene divinylbenzene, with Al_2O_3 via atomic layer deposition (ALD) using trimethyl aluminum (TMA) and water. Until this quarter, we have been unable to deposit significant amounts of Al_2O_3 on the DOWEX particles. The low amount of Al_2O_3 we were able to deposit, shown in Figure 11, results in no mechanical stability of the shells after the polymer was removed. We attribute this to the lack of reactive sites on the DOWEX particles, which limits attachment of TMA to the particle surface (hence, inability to nucleate on the surface). We have, therefore, functionalized the surface with N_xO_y moieties using nitric acid and a combination of nitric and sulfuric acid. The setup and resulting particles are shown in Figure 12(a).

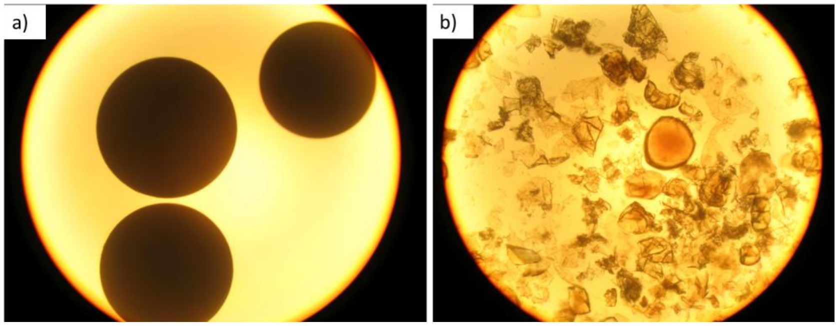

Figure 11. DOWEX particles (a) before and (b) after Al_2O_3 shells coating and burnout.

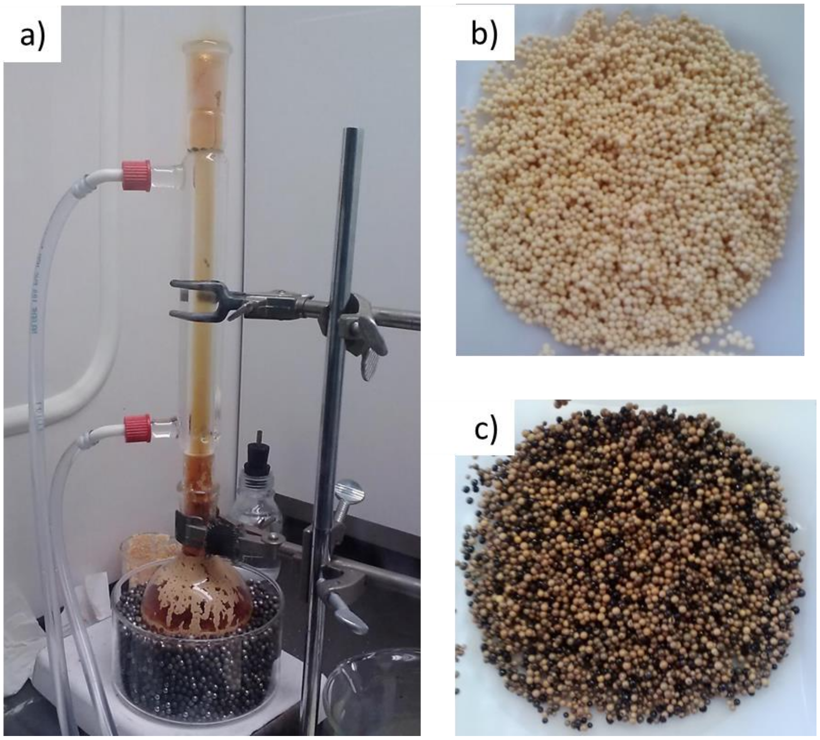

Figure 12. (a) Experimental apparatus for functionalizing DOWEX apprentice. (b) Treatment with nitric acid. (c) Treatment with 50/50 mixture of sulfuric acid and nitric acid.

The DOWEX particles were placed in the acid solution, heated to ~120 °C, and refluxed for 5 to 7 hours. As Figure 12(b) shows, the color of DOWEX particles treated with nitric acid changes from pure white to yellow, while the mixture of sulfuric and nitric acid results in both yellow and black particles, as shown in Figure 12(c). The functionalized particles serve as a much better base material for the deposition of Al_2O_3 by ALD. Skeletal Al_2O_3 substrates made by deposition on the functionalized particles maintain their spherical shape after polymer burn-out, as shown in Figure 13. Further functionalization by ALD to deposit $CoFe_2O_4$ on the resulting skeletal materials will be done in the next quarter.

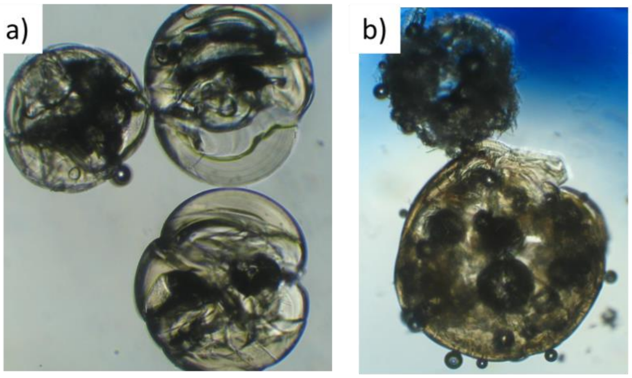

Figure 13. Skeleton scaffolds fabricated by ALD of Al_2O_3 on functionalized DOWEX particles after polymer burn-out. (a) Particles functionalized by nitric acid. (b) Particles functionalized by nitric and sulfuric acid.

Complementary to the work on synthesizing Al_2O_3 skeletal materials, we have been optimizing methods for the deposition of CoO and Fe_2O_3 by ALD in order to deposit various stoichiometries of $CoFe_2O_4$ on Al_2O_3 to synthesize active materials, as discussed above. We have successfully carried out ALD of both CoO and Fe_2O_3 on commercial alumina supports as demonstrated by the "precursor breakthrough" seen in the mass spectrometer trace of product and reaction gases (Figure 14). Precursor breakthrough occurs when all of the available surface sites have reacted and, therefore, the product gases cease to be produced and precursor molecules break through the fluidized bed. This process can then be seen in the mass spectrometer traces by a sudden decrease in the product gas concentration, CO_2 in this case, and an increase in precursor composition, either O_2 or a metallocene fragment (mass to charge ratio of 38). While we have been able to see true ALD of both CoO and Fe_2O_3, the deposition ratios we have achieved are not the 1:2 desired for the hercynite cycle. As Table 2 shows, the material we have produced to this point is deficient in CoO.

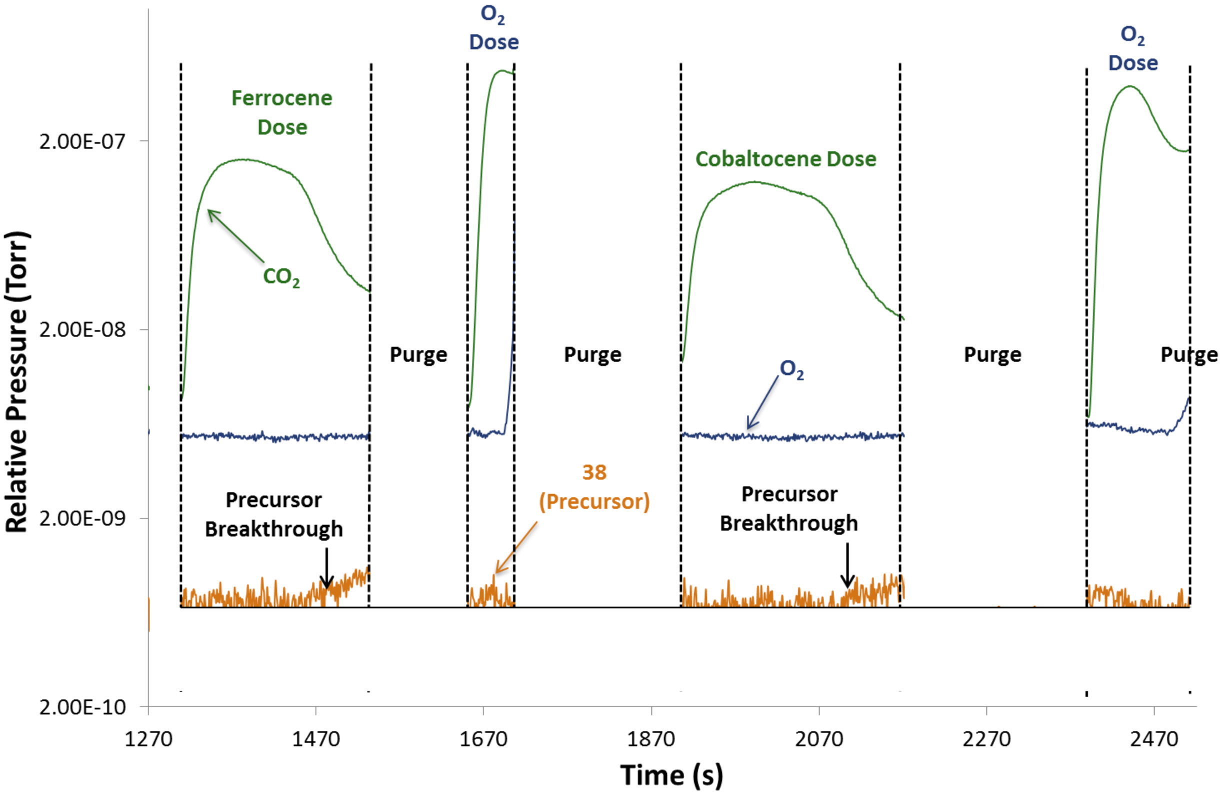

Figure 14. Mass spectrometer traces of CO_2, O_2 and metallocene fragment during an Fe_2O_3 deposition.

Table 2. The mass and mole compositions of two ALD runs carried out on commercial Al_2O_3 catalytic supports.

Number of Cycles	%	Co	Fe	Al
15	wt. %	0.69	4.4	49.2
	mol %	0.25	1.6	38.2
10	wt. %	0.35	4.0	44.2
	mol %	0.12	1.5	34.3

Testing of the active material for WS properties has focused on the steam pressure effects this quarter. ITWS is carried out at temperatures above the minimum reduction temperature by first flowing an inert gas through the reactor to sweep away generated O_2, the reduction step, and subsequently injecting steam into the system, the oxidation step. ITWS carried out at 1,350 °C is shown in Figure 15. The hercynite cycle particles are reduced for one hour and produce an average of 102 ± 18 µmol of H_2 per total gram of material. ITWS at 1,350 °C produces more O_2 and H_2 than 1,350/1,000 °C Temperature-Swing Water Splitting (TSWS), and slightly more O_2 and H_2 than even 1,500/1,200 °C TSWS, as shown in Table 3. The higher WS production capacity appears to arise from a higher H_2 production peak rate—0.55 ± 0.16 µmol of H_2 per total gram of material per second—than occurs during TSWS. However, transport effects need to be accounted for in the final analysis. A comparison of data is made with CeO_2 redox using the same system. However, while production rates and total gas-splitting capacity increase in ITWS, O_2 and H_2 production are no longer completely separated. During steam injection, after the majority of the total H_2 is generated, O_2 levels in the system begin to rise and stabilize at 7.34×10^{-3} μmol of O_2 per gram of material per second. When we stop injecting steam into the system, the O_2 production rate increases dramatically to its peak rate of 0.1 μmol/total g/s. We suggest that the slight simultaneous production of O_2 and H_2 begins when the herycnite cycle material is nearing complete oxidation, and then we see competition from reduction at these high temperatures. The dangers and expense of having to separate O_2 and H_2 produced simultaneously can be avoided in an industrial setting by halting steam injection before the oxidation reaction is complete.

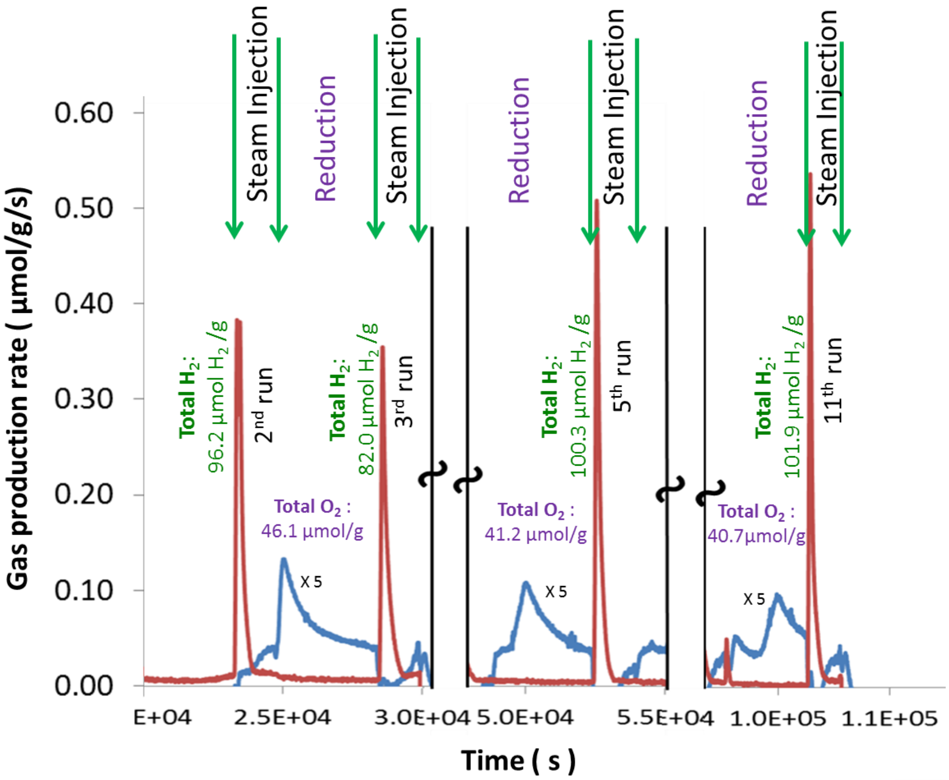

Figure 15. Isothermal WS carried out at 1,350 °C. Hercynite material was reduced for an hour, and oxidized for 25 min. in 50% steam environment at 760 Torr.

Table 3. Total quantities and peak production rates of TSWS CeO_2 and hercynite, and hercynite ITWS water-splitting cycles.

Temp Swing & Isothermal (Red/Ox)	CeO_2 (μmole/g)	Nanostructured Hercynite (μmole/total g)	CeO_2 Peak Rate (μmole/g/s)	Nanostructured Hercynite Peak Rate (μmole/total g/s)
1,500/1,200	159.1 ± 15.7	93.7 ± 19.2	1.28 (avg)	0.32 (avg)
1,350/1000	16.4 ± 3.6	31.4 ± 2.3	0.15 (avg)	0.03 (avg)
1,350/1,350		102 ± 18		0.55 ± 0.16

An increased partial pressure of water, brought about by increasing the amount of steam in the inert carrier gas, results in greater total H_2 production at higher rates than at lower steam partial pressures, as shown in Figure 16. Steam partial pressures of 253.3, 325.7 and 380 Torr (33%, 43% and 50% steam flowing through the system) correspond to H_2 production capacities of 40 ± 9, 72 ± 8, and 102 ± 18 μmol H_2 /total gram and production rates of 0.06 ± 0.02, 0.15 ± 0.07, and 0.35 ± 0.18 μmol H_2 /total gram/s, respectively. The increased production rates correspond to shorter oxidation times, as expected. The higher steam pressure results in a higher water chemical potential on the hercynite cycle particles, which provides the thermodynamic driving force for the oxidation reaction. Although a 380 Torr steam partial pressure outperforms 1,500 ^{o}C/1,200 ^{o}C hercynite TSWS in terms of H_2 production, oxidation to produce H_2 at the lower steam partial pressures does not. This suggests that by increasing the surface chemical potential of the oxidizing gas, i.e., by increasing the partial pressure of steam, we can continue to increase the ITWS temperature. Further, the higher temperature increases the oxidation kinetics rate and decreases the time required for complete oxidation.

All hercynite cycle materials were aged samples and had been cycled at least 150 times prior to the experiments discussed here. It is important to note that the hercynite cycle material is only 47% active by mass (53% is inert Al_2O_3). Hence, in order to compare activity to other monolithic active materials such as ceria, one needs to multiply the production and peak rates by a factor of 2.13. Efforts are underway to evaluate the impact of increasing active % on measured production/rates and on the structural integrity of the hercynite cycle materials during redox.

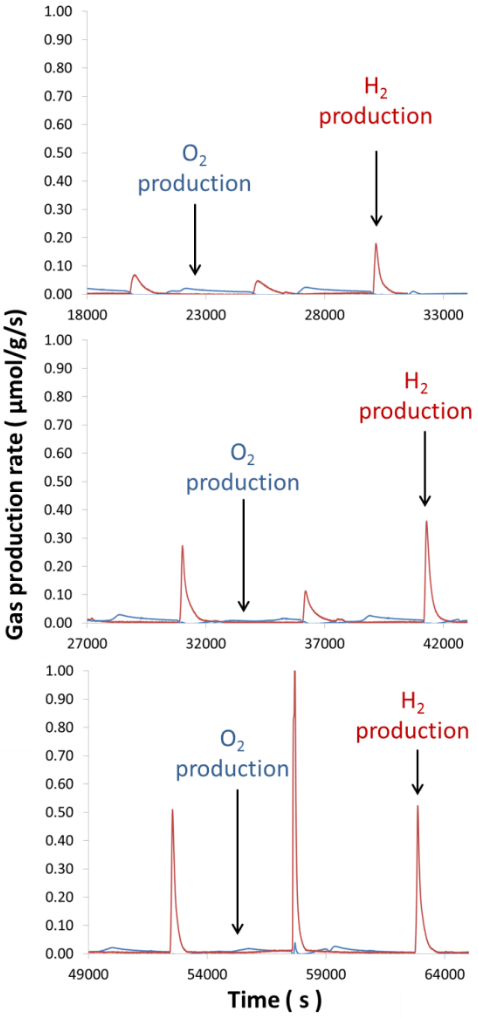

Figure 16. The effect of pressure on isothermal redox water splitting. The top graph shows a 33% steam concentration, the center graph shows a 43% steam concentration, and the bottom graph shows a 50% steam concentration. The peak rates are impacted by inconsistencies in the steam feed resulting from a less-than-desirable method of feeding steam.

Density Functional Theory (DFT) Modeling

Computational work for the past quarter has focused on utilizing the HSE density functional, determined to be necessary for accurately modeling the ferrite materials employed in ITWS, to calculate proper lattice parameters and anti-ferromagnetic structure. While HSE more accurately represents the material, the time required for the 2×2×2 K-point mesh is too expensive and time-consuming for practical use (only 20 scf steps in 24 hours). Therefore, we have decided to use HSE only for determining the lattice parameters and anti-ferromagnetic properties that are imperative to describe accurately. These supercell properties can then be matched using less expensive density functionals (PBE+U). Properties and kinetic parameters of interest will be computed at the PBE+U level with the HSE supercell configurations. Eventually, we will carry out single-point HSE calculations at the DFT+U geometries, because the difference between DFT+U and HSE geometries is minimal, but the resulting HSE energies are more accurate.

Utilizing this method, we have calculated the cation migration energy from one octahedral site to another. We have only fully converged octahedral-octahedral hopping. Rough octahedral-tetrahedral and tetrahedral-tetrahedral hopping was initially investigated, but the barriers were much higher (at least 1 eV). A cation hops from one octahedral-octahedral site to another through a tetrahedral meta-stable site, as shown in Figure 17. As Figure 18 shows, there is a clear trend between migrating cation, and unit cell size and activation barrier. Fe has the lowest activation barriers, followed by Co, followed by Ni. This ordering is a result of the octahedral-tetrahedral preference of the migrating cation. The octahredal/tetrahedral site preference arises from uneven splitting of the e_g and t_{2g} orbitals of the migrating cation, where there is a larger splitting for Ni, a medium splitting for Co, and the smallest splitting for Fe. These same concepts explain the inverse spinel nature of magnetite, cobalt ferrite and nickel ferrite, a longstanding materials science question.

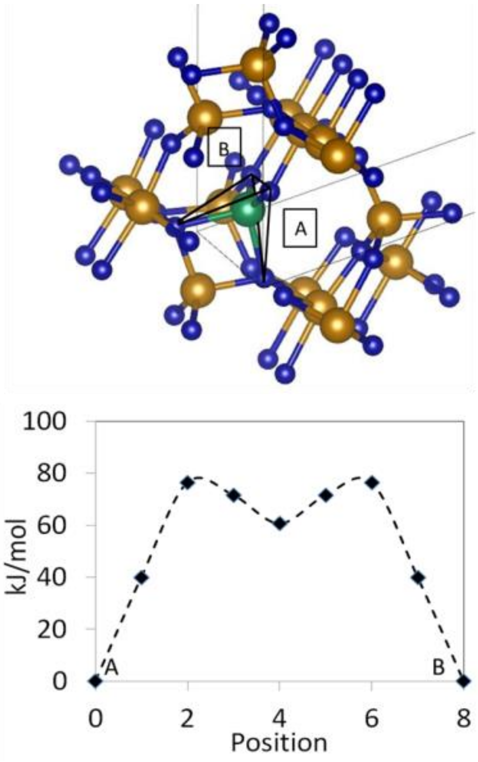

Figure 17. The NEB pathway for cation migration from one octahedral site to another. Top: transition state with the migrating ion shown in green, and initial and final positions shown as A and B square boxes. Bottom: energies along the NEB pathway.

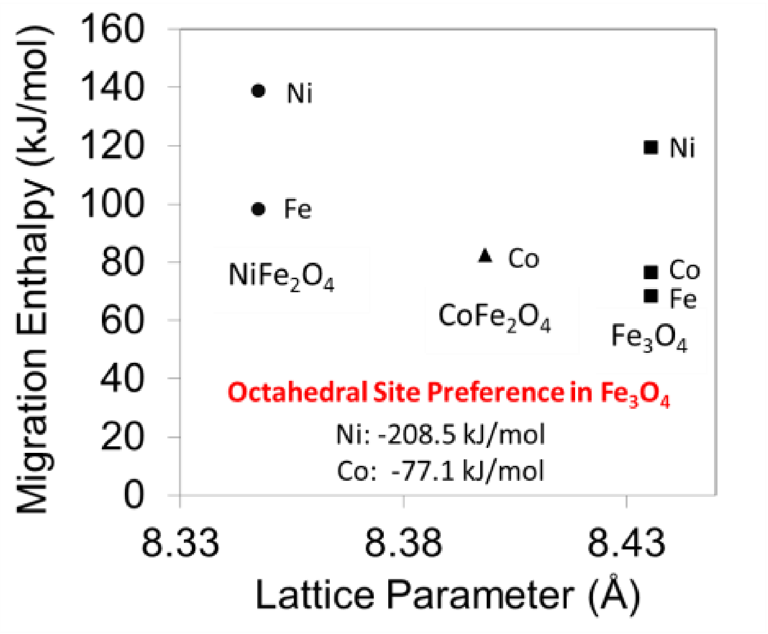

Figure 18. Hopping energy activation barrier for Ni, Co, and Fe cations at the lattice parameters of the spinel through which the cation is migrating.

PLANS FOR NEXT QUARTER AND KEY ISSUES

The plans for the next quarter are as follows: (1) finish production of the large batch of hercynite material, (2) look at dependencies of reduction time, and determine how high we can push the temperature of ITWS, and (3) investigate H_2O adsorption on the surfaces of interest with DFT.

We are currently optimizing the CoO to Fe_2O_3 ALD cycle ratios required to obtain a 1:2 Fe:Co ratio in the resulting films using commercial Al_2O_3 as a support. We are also finalizing production of the Al_2O_3 skeletal materials that will serve as materials in future experiments. We are using surface functionalized materials and depositing varying thicknesses of alumina. These will allow us to determine the minimum thickness for a mechanically sound particle as well as optimal thicknesses/chemical stoichiometry for use in WS.

Over the course of the next quarter we will investigate the dependence of reduction times (hold times of 60, 30, 10 and 0 min) on the extent of reduction and H_2 generation capacity. Given the time, we will begin further study to determine the maximum reduction temperatures that we can achieve (can we go up to 1,600 °C?). We will investigate H_2 production at both the mid-range temperature used for the reduction study as well as the upper temperature determined in the temperature study. Low temperatures will not be tested as these are dictated by reduction and not H_2O oxidation. Additionally, we will run 10 cycles continuously on the same sample to attempt to explain the increasing H_2 production behavior seen for the nanostructured hercynite cycle material.

DFT simulations will continue on to surface studies, and migration studies will extend to aluminates in addition to the ferrites explored this quarter. DFT + U calculations will be used to determine the most likely surfaces and HSE calculations will verify this by re-calculating the energies of the two or three most stable surfaces. From these surfaces, the adsorption energies of H_2O, H_2, and O_2 will be calculated. Subsequently, H_2O dissociation and H_2 formation energies will be calculated using the Nudged Elastic Band method at DFT+U levels with a final single point energy calculated at the HSE level.

MULTI-TUBE SOLAR RECEIVER

Point of contact: Alan W. Weimer

PROJECT STATUS

Multi-Tube Solar Receiver Modeling

The solar receiver consists of an array of tubular absorbers filled with the active material and contained within an insulated absorbing cylindrical outer cavity with a small aperture to admit the concentrated solar energy. A three-dimensional dynamic computational model coupling radiative transfer with fluid flow, heat transfer, mass transfer, and chemical reaction kinetics was previously developed to evaluate the performance of the solar receiver and to assess sensitivity to various physical properties and operating conditions including bed porosity, bed permeability, effective thermal conductivity, and inlet flow rates. Progress over the past quarter has focused on further utilization of the previously described computational model to assess sensitivity of “temperature swing” receiver performance to reaction kinetics and geometric parameters describing receiver design. Receiver performance was evaluated on the basis of the time-averaged solar-to-chemical efficiency defined in equation 1.

$$\overline{\eta} = \frac{\int_{cycle} \dot{n}_{H_2} LHV_{H_2} \, dt}{\int_{cycle} P_{solar} dt + \int_{cycle} E_{O_2} \dot{n}_{O_2} \, dt} \qquad (1)$$

The time-averaged solar-to-chemical efficiency represents the ratio of the heating value of the H_2 produced in a designated time period to the sum of the solar energy incident on the receiver over the same time period (defined here as one cycle) and the energy required to separate oxygen produced during the reduction from the inert. The energy required for oxygen separation is taken to be 0.5 W per 3.77 sccm O_2, consistent with that necessary for oxygen transport membranes.

Kinetic rate expressions and associated parameters are currently based on extrapolations from available literature values and will be replaced with experimentally measured values when available. Table 4 provides the sensitivity of the temperature swing receiver performance to various changes in reduction or oxidation reaction rates or activation energy with a 3-kW solar input, assumed adiabatic external cavity walls, and a receiver window actively cooled to ambient temperature. These initial calculations indicated that average H_2 production could vary by at least 20% with reasonable uncertainties in kinetic parameters. However, the relative performance between different tube configurations was found to be less sensitive to the kinetic parameters than the performance of any single given design. Figure 19 illustrates the time-averaged efficiency for each of three different tube configurations normalized to the efficiency for the configuration with four tubes. All tube configurations contained an identical amount of active material and were evaluated with identical argon or steam inlet flow rates. Calculations were repeated with the activation energy for the reduction reaction reduced by 15% and with the overall rate of the oxidation reaction reduced by a factor of 10. The relative change in performance between the tube configurations was nearly independent of the oxidation rate. Slightly larger discrepancies were observed with the ten-tube configuration when the reduction activation energy was reduced.

Table 4. Sensitivity to reaction rates.

Property	Property Change	Change in Average H_2 Production
$R_{reduction}$	×10	+21%
Ea_{red}	-15%	+18%
R_{OX}	×0.1	-12%

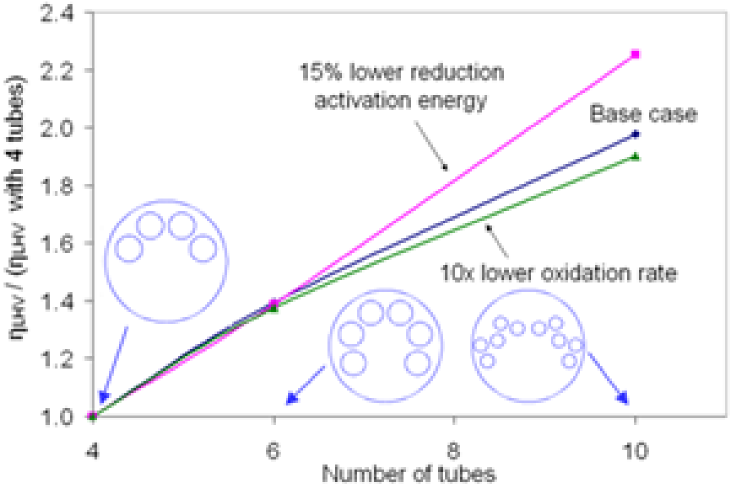

Figure 19. Time-averaged efficiency for each of three different tube configurations normalized to the efficiency for the configuration with four tubes.

Alternative tube configurations and interactions between tube configuration, operating conditions, and solar beam shape and directionality were assessed for the temperature swing design via a resolution IV 2^{15-10} fractional factorial design. Nine factors controlled the geometrical tube array configuration and included the number of tubes, total tube cross-sectional area, bed height, aperture size, spacing between tubes, spacing between "hot" and "cold" tubes, staggered/unstaggered tube arrangements, radius of curvature of the tube semicircle, and distance between the tube array and the aperture.

Three additional factors defined the Gaussian shape of the solar flux profile at the aperture, the total beam width, and the beam aim point. For each tube arrangement the beam width and aim point were initially optimized on the basis of maximizing uniformity in solar absorption between tubes on the “hot” side of the receiver while simultaneously minimizing solar energy absorbed on the “cold” side. The beam width/aiming factors then represented deviations from the optimum based on solar absorption.

The final three factors were the cycle time, and steam or inert flow rates defined as the inlet velocity at standard conditions. All designs were evaluated with a 4-kW solar input, adiabatic external walls, and an imposed window temperature of 800 °C. Predicted receiver efficiency for the set of 32 designs ranged from 4–18%. Figure 20 shows the main effects and binary interactions resulting from the fractional factorial design analysis. Receiver performance was largely controlled by the amount of active material (via the total tube cross-sectional area), the aperture size, and the steam flow rate. Emissive losses through the aperture are the dominant mode of heat loss, in some cases accounting for more than 50% of the input solar power. Thus, a smaller aperture is strongly preferred.

Parameters purely describing tube placement appear to have little impact on performance, as radiative exchange within the cavity led to relatively uniform temperature distributions. Parameters describing beam width and aiming also produced little impact, indicating that, for any given tube configuration, optimal beam size and shape can be determined on the basis of solar absorption alone without consideration of receiver temperatures and H_2 or O_2 production rates. Cycle time produced only a small impact on receiver efficiency over the 6–12 minute range considered, as it was imposed independently of reaction kinetics. The short cycle time led to a roughly proportional decrease in H_2 production per cycle as the active material cycled within a smaller range of reduction/oxidation states. These effects are currently being evaluated with an increased steam flow rate in order to assess the significance of design parameters on a more uniform basis.

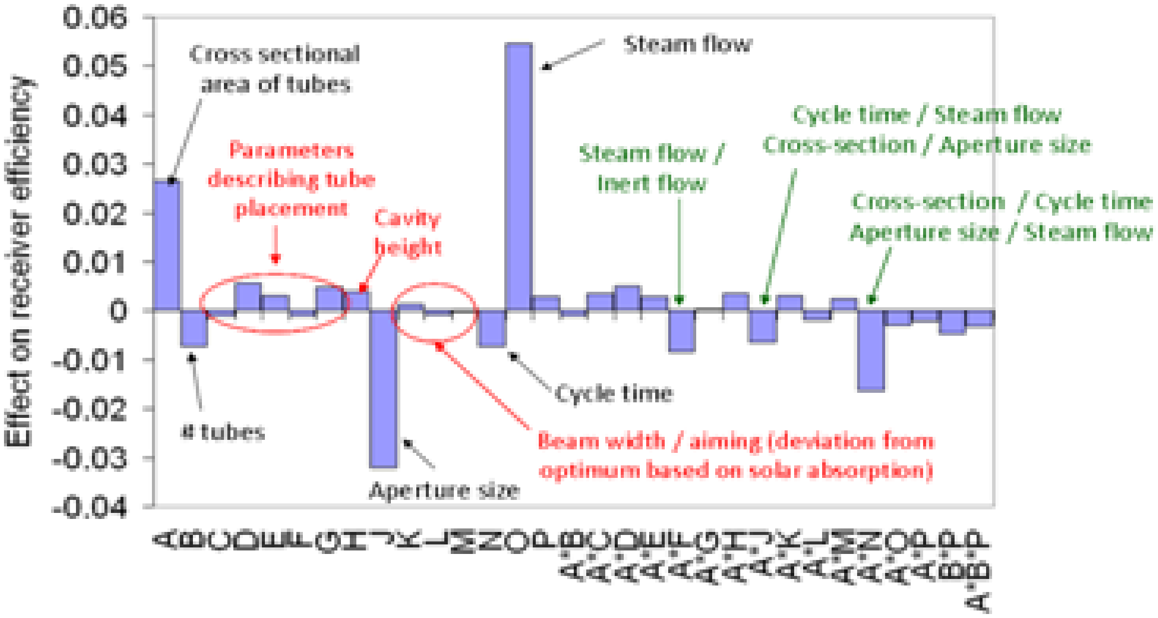

Figure 20. Main effects and binary interactions from 2^{15-10} fractional factorial design.

On-Sun Redox Demonstration

On-sun testing is scheduled to begin early summer using the materials synthesized in the lab. Prior to on-sun testing of the synthesized materials, the reactor operated previously by students in the group will be checked out, and any necessary repairs and/or modifications necessary for isothermal water splitting testing will be made.

PLANS FOR NEXT QUARTER AND KEY ISSUES

Planned work to be carried out over the next quarter will involve further investigation of alternative tube configurations. The results described above indicate that receiver performance is controlled by a small number of parameters, particularly the active material cross-sectional area, aperture size, and number of tubes. This subset of parameters will be investigated in more detail via a response surface design to identify potential optima in efficiency. Similar sets of calculations will then be carried out for the isothermal design, thereby allowing detailed comparison of the performance between temperature swing and isothermal operation on the basis of an ideal receiver configuration for each design.

PUBLICATIONS/PRESENTATIONS

Scheffe, J.R., A.H. McDaniel, M.D. Allendorf and A.W. Weimer, "Kinetics and Mechanism of Solar-Thermochemical H_2 Production by Oxidation of a Cobalt Ferrite-Zirconia Composite," *Energy & Environmental Science*, **6**, 963-973 (2013).

Liang, X.H., B.W. Evanko, A. Izar, D.M. King, Y.-B. Jiang and A.W. Weimer, "Ultrathin Highly Porous Alumina Films Prepared by Alucone ABC Molecular Layer Deposition (MLD)," *Microporous and Mesoporous Materials*, **168**, 178-182 (2013).

Martinek, J. and A.W. Weimer, "Design Considerations for a Multiple-Tube Solar Reactor," *Solar Energy*, **90**, 68-83 (2013).

Weimer, A.W., J.R. Scheffe, P. Lichty, C. Perkins, and S.M. George, "Metal Ferrite Spinel Energy Storage Devices and Methods for Making and Using Same," U.S. Patent 8,397,508 (2013).

Weimer, A.W. et al., "Nano-Engineered Particles for Solar Thermochemical CO_2/H_2O Splitting," paper presented at the PARTEC 2013 International Conference, Nuremberg, Germany, April 24, 2013.